García-Rodríguez, N., Campos, M., Torralba, J. M., Berger, M. H. & Bienvenu, Y. (2014). Capability of mechanical alloying and SPS technique to develop nanostructured high Cr, Al alloyed ODS steels. *Materials Science and Technology*, 30(13), 1676-1684.

DOI: 10.1179/1743284714y.0000000595

Capability of mechanical alloying and SPS technique to develop nanostructured high Cr, Al alloyed ODS steels

N. García-Rodríguez*[1], M. Campos[1], J. M. Torralba[1,2], M. H. Berger[3] and Y. Bienvenu[3]

Oxide dispersion strengthened (ODS) Fe alloys were produced by mechanical alloying (MA) with the aim of developing a nanostructured powder. The milled powders were consolidated by spark plasma sintering (SPS). Two prealloyed high chromium stainless steels (Fe–14Cr–5Al–3W) and (Fe–20Cr–5Al + 3W) with additions of Y_2O_3 and Ti powders are densified to evaluate the influence of the powder composition on mechanical properties. The microstructure was characterised by scanning electron microscope (SEM) and electron backscattering diffraction (EBSD) was used to analyse grain orientation, grain boundary geometries and distribution grain size. Transmission electron microscopy (TEM) and scanning transmission electron microscopy (STEM) equipped with energy dispersive X-ray spectrometer (EDX) were used to observe the nanostructure of ODS alloys and especially to observe and analyse the nanoprecipitates. Vickers microhardness and tensile tests (*in situ* and *ex situ*) have been performed on the ODS alloys developed in this work.

Keywords: Material nanostructured, Oxide dispersion strengthened, Mechanical alloying, Spark plasma sintering

This paper is part of a special issue on …

Introduction

Conventional high Cr ferritic/martensitic (FM) steels have long been used in different structural elements for nuclear applications and fossil fired plants. Despite some good mechanical properties of the FM steels, the upper operating temperature is limited to 550–600°C. One alternative to increase the maximum operating temperature and to keep the advantages of the FM steels would be the development of oxide dispersion-strengthened (ODS) ferritic steels[1,2] In addition, prior studies have concluded that controlling the alloying elements is possible to design alloy compositions for corrosion resistant ODS ferritic steels and with better mechanical properties.[3]

Therefore, several alloying additions are required to produce the desire combination into the matrix brings obstacles to the motion of properties for the ODS ferritic steels. The introduction of Y_2O_3 particles into the matrix develops nanoparticles which block the motion of dislocations to improve the high temperature strength.[4] Besides, the addition of an active element such as Ti can result into a refinement of the microstructure and to the development of non-stoichiometric Y–Ti–O nanoclusters can be achieved[5,6] Cr and Al are added to improve the corrosion resistance of ODS steels. For the optimization of Cr content the balance between the advantage of corrosion resistance and the inconvenient of increasing of the susceptibility to aging embrittlement through the formation of Cr-rich secondary phases[7] should be considered. An Al addition can form an alumina layer, especially at high temperatures, as well as can be an effective element to obtain Y–Al oxide particles in a Fe–Cr–Al matrix.[8] In spite of this, it is necessary that both elements have an adequate combination in content ranges to optimise the properties.[3] Finally, W is an effective element for solid solution strengthening to provide the required mechanical properties and to enhance the stability of α-ferrite phase.[9]

The mechanical alloying method (MA) is selected to produce the ODS ferritic steels, with the aim of developing a nanostructured powder with a proper intimate mixture between the base metal and the reinforcing particles.[10] In order to keep the fine structure of the MA-powders, spark plasma sintering (SPS) technique was used to consolidate the milled powders. The advantages of the SPS method are its high thermo-efficiency as well as the fast heating-up of the sample to high temperature avoiding grain growth or nanoprecipitation coarsening.[11] Thus, the scope of this paper is to study the capability of

SPS technique to produce nanostructured materials and nano-precipitates from the structure of milled powders.

[1]Universidad Carlos III de Madrid, Av. Universidad 30, 28911 Leganés, Madrid, Spain
[2]IMDEA Materials Institute c/Eric Kandel, 2, Tecnogetafe, 28906, Getafe, Madrid, Spain
[3]MINES ParisTech, Centre des Matériaux, CNRS UMR 7633, BP 87, 91003 Evry Cedex, France

*Corresponding author, email ngrodrig@ing.uc3m.es

Published by Maney on behalf of the Institute
Received 6 March 2014; accepted 17 June 2014
DOI 10.1179/1743284714Y.0000000595

Experimental procedure

In this work, two ODS steels powders were produced by high energy milling from two different prealloyed grades. The composition of the prealloyed and ODS powders can be found in Table 1 and it can be seen that that the alloying elements are introduced either in the prealloyed powder or as elemental powder addition. Mechanical alloying (MA) was performed in a ZOZ Attritor Simolayer CM01, under high purity argon atmosphere (99·9995 vol.-%) with constant flow after vacuum purge ($\approx 10^{-3}$ mbar). The rotating speed was 900 rev min^{-1} for 30 h with a ball-to-powder weight ratio 15 : 1 and using diameter 5 mm balls. All powder handling was done in a glove box under argon. The D50 particle size parameter of prealloyed powders and ODS powders after milling process is showed in Table 1. The milled powders were consolidated by SPS in order to produce compacts of 20 mm diameter and 6 mm thickness. The maximum temperature and compressive stress applied during the SPS process were 1200°C and 64 MPa respectively. These parameters are maintained during 15 s, the time of the complete SPS cycle was 35 min. The densities of the consolidated samples were measured by Helium pycnometer (AccuPyc II 1340).

The interstitial elements content (O, N and C) were quantified using a combustion analyser model LECO TC500 for O and N content and LECO CS230 for C. The crystallite size and microstrain data have been obtained by Scherrer Method using the X'pert Highscore software through X-ray diffraction patterns collected on an *X'pert* Phillips using CuKα radiation. The microstructure of alloys were investigated using SEM (Phillips XL-30), EBSD detector (FEI Nova NanoSEM 450 SEM/EBSD) and TEM (Tecnai F20 electronic transmission electron microscope). In this work, EBSD sampling points were recorded with a step size of 50 nm, with a minimum grain size (which defines the number of points required to decide whether a given group of points should be considered a 'grain' group) of 2 nm. The grain tolerance angle, which means that two neighbouring scan points belong to the same grain if the misorientation between them is less than some value prescribed by the user, was of 5° degrees. Specimens for scanning electron microscopy were ground and polished by means of standardised techniques for metallographic examination and a solution of 15 mL HCl + 2·5 g $FeCl_3$ has been used to reveal the microstructure. The specimens for EBSD characterization were further fine polished with 0·05 μm colloidal silica solution. TEM samples were prepared by electropolishing 3mm disc using 45% butoxyethanol + 45% acetic acid + 10% perchloric acid as electrolyte at room temperature.

Table 1 Nominal compositions (wt-%) of prealloyed powders, ODS powders milled and particle size d_{50}*

Nomenclature	Fe	Cr	Al	W	Ti	Y_2O_3	d_{50}/μm
14Al	78·00^{P}	14^{P}	5^{P}	3^{P}	…	…	29·8
14Al–ODS–Ti	77·35^{P}	14^{P}	5^{P}	3^{P}	0·4^{E}	0·25	49·3
20Al	75·00^{P}	20^{P}	5^{P}	…	…	…	15·7
20Al–ODS–Ti	71·35^{P}	20^{P}	5^{P}	3^{E}	0·4^{E}	0·25	98·2

*Alloying method: ^{P} Prealloyed; ^{E} Elemental powder.

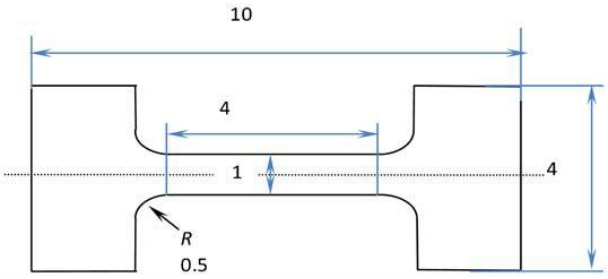

1 Sketch of tensile specimen geometry (dimensions are in mm)

The Vickers microhardness of specimens was measurement using a 200 g load at room temperature with a dwell at maximum load of 15 s. Each result is the average of 5 × 3 matrix measurements.

Tensile tests were conducted using miniature dog-bone specimens Fig. 1. The unusual gauge length forces to calculate the strain from the crosshead displacement. This specimen geometry assures a uniform deformation.[12] Tensile load was applied with a rate of 2 μm s^{-1}.

Results and discussion

A chemical analysis of interstitial elements of the milled powders and the samples consolidated were performed to evaluate the degree of contamination associated with the mechanical alloying and SPS process. Table 2 shows the content in oxygen, nitrogen and carbon of prealloyed starting powders and ODS alloys and suggests that these results show that the interstitial elements content in the powders increases with the milling process although it is performed under pure Ar.[13] The carbon contamination is kept similar after consolidation process indicating that the SPS technique is not producing a significant contamination. Regarding the oxygen and excess oxygen (Ex.O) contents, a decrease in the values has been produced after SPS process. The Ex. O is an important parameter to predict the oxide particle distribution or to estimate total amount of oxide particles in ODS with Ti. Thanks to the decrease produced in the oxygen content after the consolidation, it is possible to achieve the value that Ohtsuka *et al.*[14,15] estimate as adequate to obtain a good properties in the developed ODS.

To retain a nanostructure in the SPS consolidated samples it is important to ensure high microstrain and low crystallite size values after milling. During the

Table 2 Chemical analysis of oxygen, nitrogen and carbon for initial prealloyed powders, mechanical alloyed ODS powders and consolidated samples (SPS)

	%C	%O	Ex. O*	%N
14Al (powder)	0·012	0·029	…	0·007
14Al (SPS)	0·013	0·056	…	0·014
14Al–ODS–Ti (powder)	0·141	0·350	0·297	0·220
14Al–ODS–Ti (SPS)	0·128	0·142	0·094	0·061
20Al (powder)	0·002	0·063	…	0·029
20Al (SPS)	0·032	0·012	…	0·074
20Al–ODS–Ti (powder)	0·093	0·157	0·104	0·033
20Al–ODS–Ti (SPS)	0·109	0·149	0·096	0·045

*Ex. O is excess oxygen (defined as total oxygen contents in steel minus oxygen content in Y_2O_3).

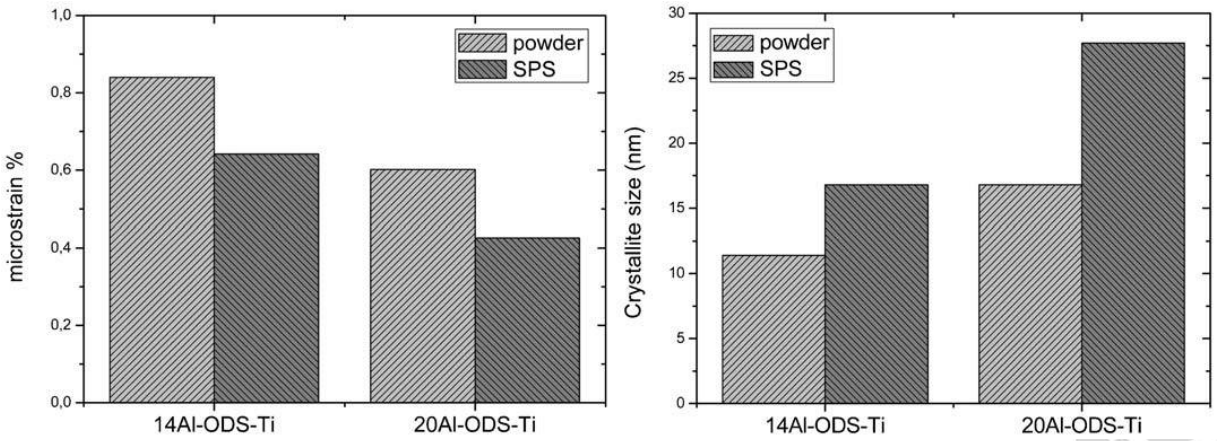

2 Comparison of microstrain and crystallite size of 14Al–ODS–Ti and 20Al–ODS–Ti alloys before and after consolidated by SPS

consolidation process the thermal activation will lead to crystallite growth, but internal strain decreases below a certain value that depends on the material.[16,17] Only when the system is relaxed, the crystallite size grows. This fact is observed when the microstrain and crystallite size of ODS alloys is comparable before and after consolidated (Fig. 2). The crystallite size of SPS samples is bigger than that of powder samples for both ODS alloys due to the decrease produced in microstrain after the SPS process. Even so, the SPS samples keep nanostructured features.

After the SPS consolidation, high densities for both materials processed have been obtained (Table 3) which indicates the efficiency SPS technique. In all the cases a relative density higher than 98% is reached.

Microstructure characterisation

SEM examinations

The microstructures of prealloyed samples (14Al and 20Al) and 14Al–ODS–Ti and 20Al–ODS–Ti alloys after the SPS consolidation are shown in Fig. 3. The prealloyed samples show equiaxiaed grains and 20Al prealloyed microstructure exhibits a smaller grain size than the 14Al (Table 1).However, the SEM study reveals a refinement in grain size and an elongated morphology inherit from the mechanical alloying process in both ODS alloys. Also, a dispersion of elongated precipitates is observed with a preferential localisation near grain boundaries, but a quantification of those precipitates is difficult since their distribution is far from homogeneous. Their chemical nature was investigated by EDS semiquantitative analysis. The analysis reveals that the precipitates are complex carbides type MC and M_2C of Cr and W. The carbon necessary for the formation of theses carbides can be mainly attributed to contamination produced during the milling process from milling tools.[18]

Table 3 Relative densities of ODS alloys consolidated by SPS*

	14Al–ODS–Ti	20Al–ODS–Ti
Relative density/%	98·58	99·99

*Theoretical density $\frac{1}{\rho_t} = \sum \frac{w_i}{\rho_i}$.

EBSD analysis

The EBSD analysis gives information on the grain size and morphology, grain crystallographic orientation and crystallographic texture. Figure 4 shows the grain orientation maps (inverse pole figure, IPF) of 14Al–ODS–Ti and 20Al–ODS–Ti alloys. Each different colour in the IPF map represents a crystallographic orientation which is related to the colour code expressed in the standard triangle. For every sample the Kikuchi patterns were indexed with ferrite phase only, and for this reason there are regions in the map where indexing of Kikuchi pattern was not possible (dotted regions) and these regions corresponding to the carbides seen in Fig. 3. The large variety of colours in the grain orientation map indicates that the SPS samples are highly isotropic.

The grain size distribution as function of grain size diameter in the form of histogram of the area scanned is shown in Fig. 5. In both alloys a heterogeneous recrystallisation and a non uniform grain growth was generated. This is due to the deformation produced in individual particles and to the variability of the precipitates produced during mechanical alloying processes. These phenomena lead to multi modal distribution of grain size with a bigger grain size in the 20 wt-%Cr alloy (84 nm–10·2 μm) than in the 14 wt-%Cr alloy (80 nm–5·3 μm), despite the starting powders with 20 wt-%Cr have smaller particle size. The large difference between the final grain sizes can be linked to the difference in the strain level produced in the milling process. In the 20Al 20Al–ODS–Ti alloy the W is added as elemental powder in the 20Al prealloyed powders (Table 1) and during milling process the solid solution of W is not totally achieved and the alloy is less strengthened. This was evidenced by TEM STEM examination of the 20Al–ODS–Ti milled powder (Fig. 6) where the bright areas (dotted line) are W particles that are not dissolved in the steel matrix. Therefore the 20Al–ODS–Ti powders suffer a higher strain hardening during mechanical alloying than 14Al–ODS–Ti powders although the first have higher chromium content. Owing to that, the 20Al–ODS–Ti alloy has a lower recrystallisation temperature and the grain growth during the SPS process will be larger.

TEM observations

TEM observations provided details of the grain structures, precipitates and dislocations developed

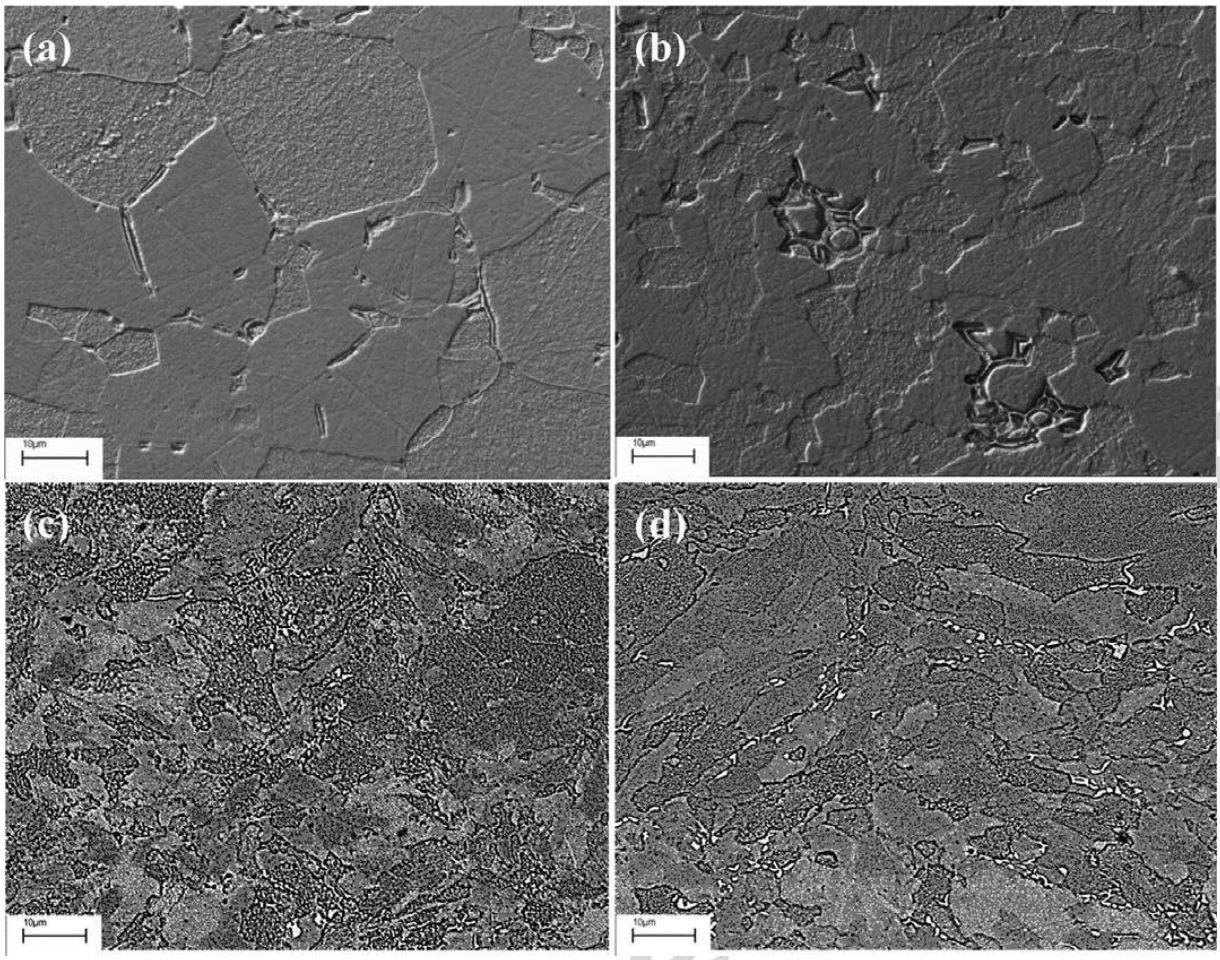

a 14Al prealloyed; *b* 20Al prealloyed; *c* 14Al–ODS–Ti; *d* 20Al–ODS–Ti

3 Images (SEM) of microstructure of ODS alloys consolidated by SPS

through the manufacture process by mechanical alloying and SPS consolidation.

Figure 7 shows the bright-field TEM images of the general microstructure observed in the 14Al–ODS–Ti and 20Al–ODS–Ti alloys. Both ODS alloys contained several types of precipitates of different size, morphology and composition. The size and nature of these precipitates, allow to group them in two categories: bigger Cr rich precipitates, and nanometric precipitates.

Figure 8*a* shows in more detail a zone with Cr rich precipitates. These large precipitates with sizes ranging from 400 to 850 nm were preferentially located at grain boundaries. Figure 8*b* shows EFTEM image where it is possible to confirm Cr rich nature of precipitates. These precipitates are very difficult to avoid because are picked

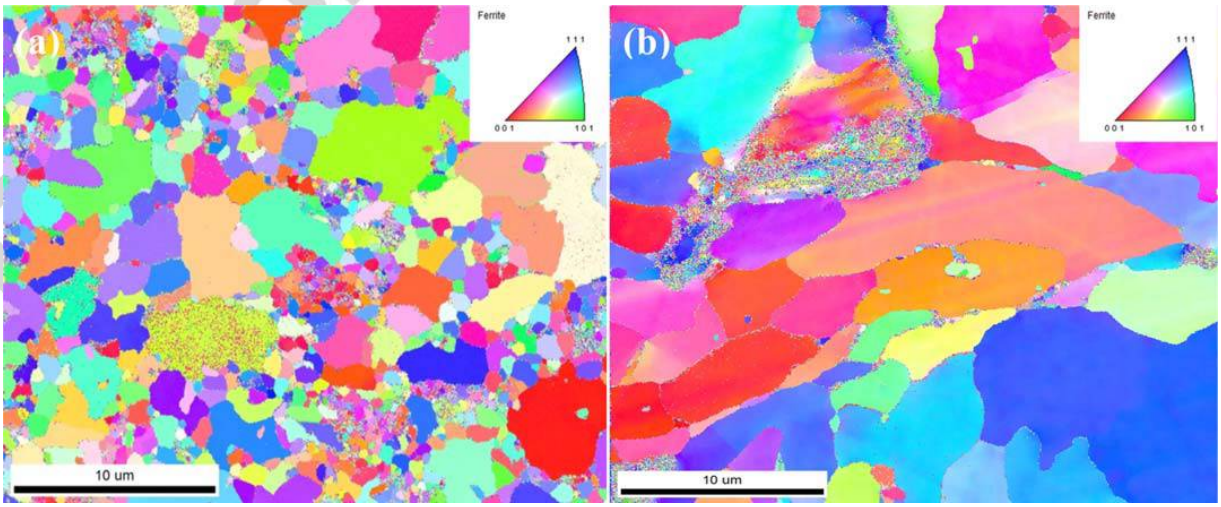

4 Inverse pole figure maps obtained by EBSD with colour key for crystallographic orientation of *a* 14Al–ODS–Ti alloy and *b* 20Al–ODS–Ti

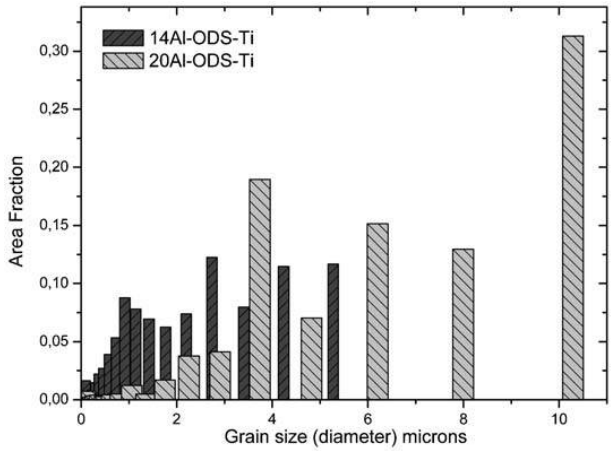

5 Comparison of grain size distribution of 14Al–ODS–Ti and 20Al–ODS–Ti alloys

up during the milling of the powders, how it has been mentioned previously.

The STEM observations (Figs. 9 and 10) show a homogenous distribution of nanoprecipitates although they have differences in composition, size and morphology. It can be observed that the composition is directly related to the size of nanoprecipitates.

Then, in 14Al–ODS–Ti alloy and 20Al–ODS–Ti alloy, attending to the composition it can be identify three types of nanoprecipitates and four types of nanoprecipitates respectively. These types of nanoprecipitates can be described and characterised as follows:

(i) type 1: the EDS analysis reveals that these particles contain Y, Al and O. These particles exhibit sizes between 10 and 50 nm and a round shape. Their location is both on grain boundaries as inside the grains. This type of nanoprecipitates exists in 14Al-ODS-Ti as in 20Al-ODS-Ti alloys

(ii) type 2: the composition of these particles is Y and O and they have a very similar size to particles type 1. They are located inside grains as well on grain boundaries, this later location being more common. Both alloys developed in this work have this type of precipitates

(iii) type 3 and 3': this type of particles enclosed Ti and W, but particles type 3' contain O as well. The size of particles Ti–W is around 75 nm with a round shape and they are in the 14–ODS–Ti

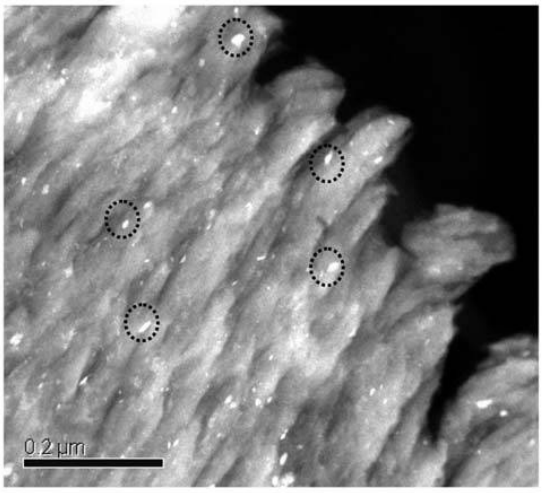

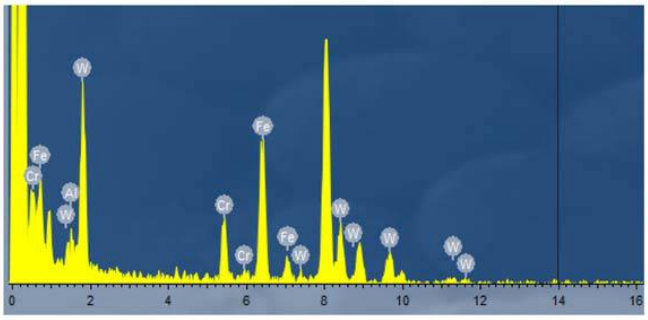

Element	Weight %	Atomic %
Fe(K)	4.57	31.28
Cr(K)	3.14	44.46
Al(K)	1.84	13.49
W(L)	**5.18**	**10.77**

6 HAADF-STEM image 20Al–ODS–Ti powder milled and EDS semiquantitative analysis

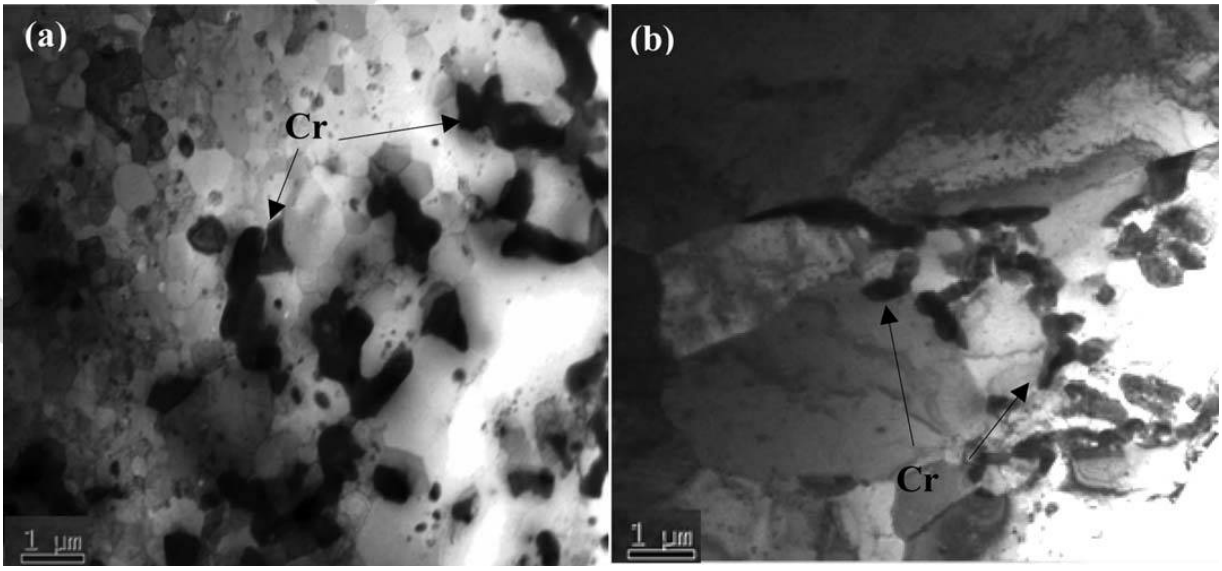

7 BF-TEM images of general microstructure of *a* 14Al–ODS–Ti and *b* 20Al–ODS–Ti

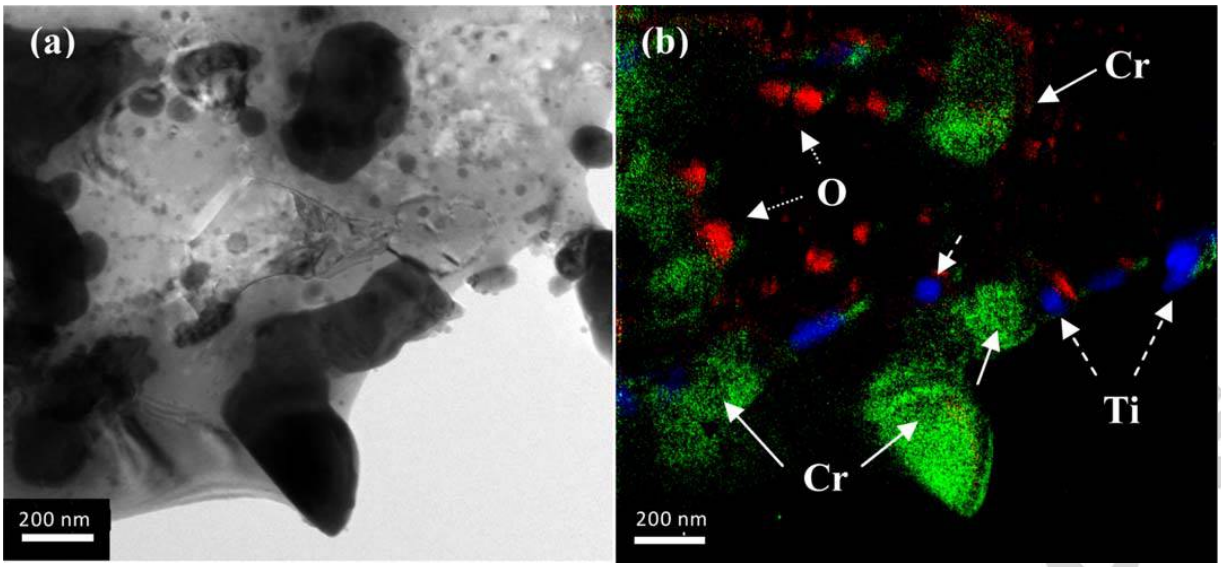

8 BF-TEM image of *a* detail of some precipitates and *b* corresponding EFTEM image of their composition

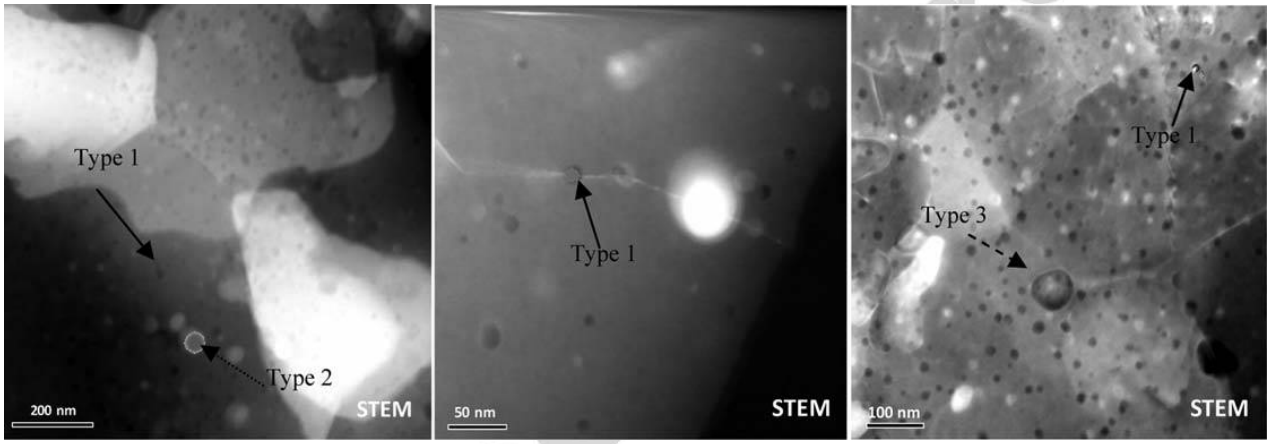

9 STEM images of 14Al–ODS–Ti alloy

alloy. The Ti–W–-O particles have an oval shape but a similar size and they are only in the 20–ODS–Ti alloy. These particles are not located on grain boundaries

(iv) type 4: these particles have only been found in the 20–ODS–Ti alloy and they enclose only Ti and O. The size, shape and location are very similar to those of nanoprecipitates type 3'.

In order to try to identify the structure of the nanoprecipitates found in both samples, a series of high resolution images with FFT analysis of the image of some oxide particles were realized (Fig. 11). We have

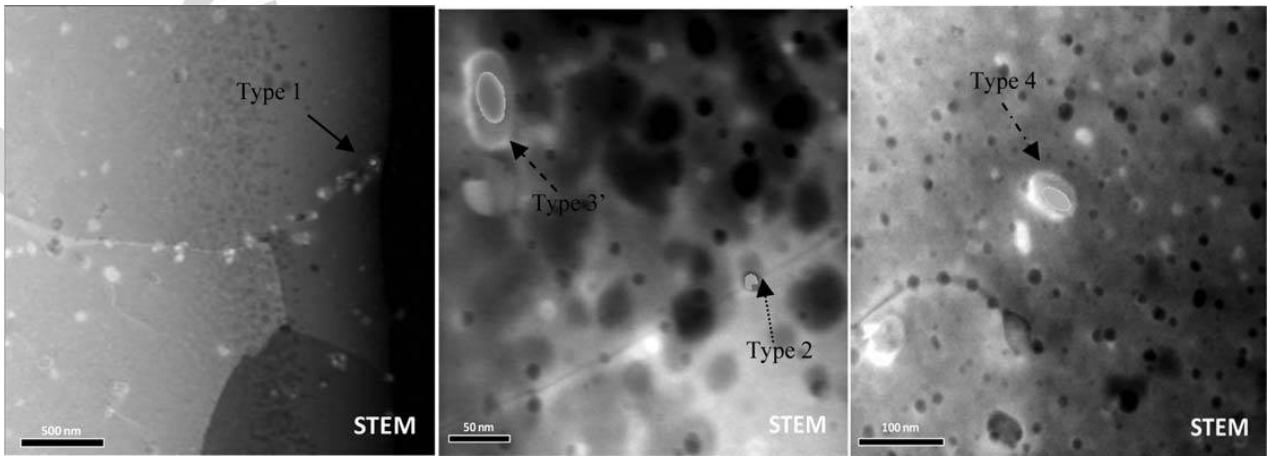

10 STEM images of 20Al–ODS–Ti alloy

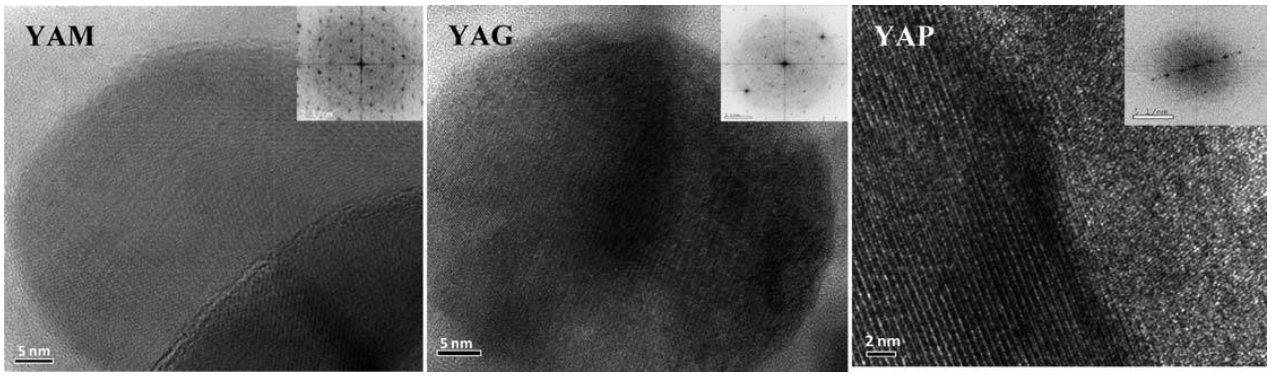

11 HRTEM images to nanoprecipitates of Y–Al–O

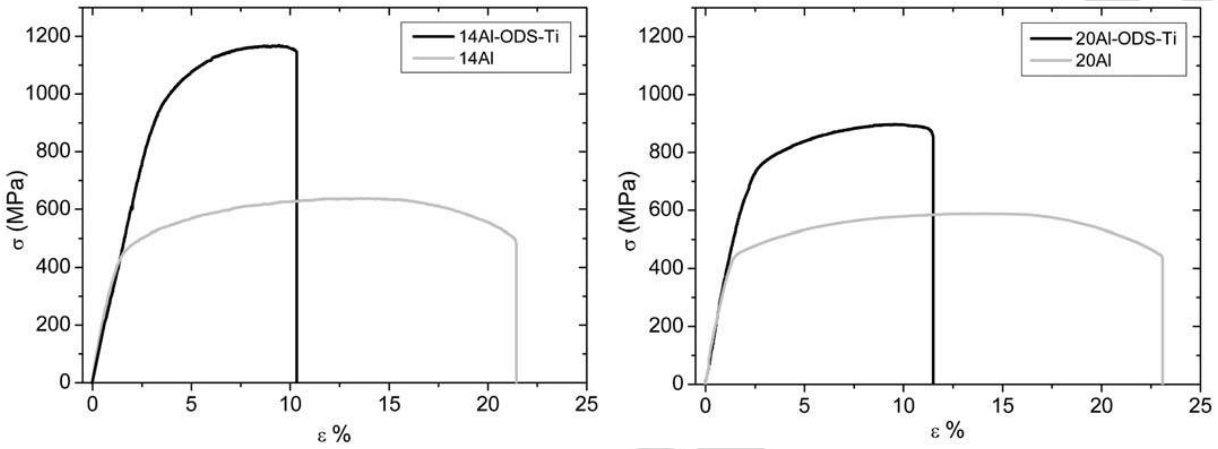

12 Tensile stress–strain curves for both ODS alloys and prealloyed consolidated

focused on the particles of Al–Y–O because they have finer scale therefore is more probable that these particles act pinning dislocations motion.[8,18] The analysis of the atomic plane spacing and angles through the FFT images indicates that the structure of these oxides could fit to those of $Y_2Al_4O_9$ (YAM), $YAlO_3$ perovskite (YAP) or $Y_2Al_5O_{12}$ garnet (YAG). The formation of these oxides implies the transformation of yttrium oxide to a mixed Y–Al–O during the milling and consolidation process.[8,19] The formation of complex nano-oxides depends of the affinity of the alloying elements with the oxygen. Therefore, in ODS steels with Al and Ti, the formation of Y–Al–O complex is more favourable than Y–Ti–O complex.[20] Other previous studies showed similar results, as Kasada *et al.* confirming that only Y–Al complex oxides can be formed when ODS FM steels contain both aluminium and titanium.[20]

Mechanical properties

Mechanical properties at room temperature were evaluated on SPS ODS consolidated alloys and the starting prealloyed powders consolidated to analyse the extent of the nanostructural modifications produced by MA and the capacity of the nanoparticle dispersion to strengthen and stabilize the grain structure of ODS alloys developed in this work.

Tensile test

Tensile tests *ex situ* and *in situ* (the SEM chamber) have been performed at room temperature. Figure 12 shows tensile stress–strain curves of ODS and prealloyed alloys. The increase of tensile strength for ODS alloys is evident with respect to the prealloyed samples being the enhancement factor for yield strength (YSODS/YSprealloyed) is larger for the 14%Cr grade than for the 20%Cr one.

Tensile properties for both alloys are compared in Table 4. Although the hardening ratio (UTS/YS) of 20Al–ODS–Ti is bigger than that of 14Al–ODS–Ti, it seems that the latter shows a larger ODS strengthening. This fact can be explained considering the 20Al–ODS–Ti has a bigger grain size than 14Al–ODS–Ti alloy (Fig. 4) and that the W addition is as elemental powder in the 20Al prealloyed, which as explained earlier, may cause a

Table 4 Tensile properties of prealloyed alloys and ODS at room temperature

	UTS/MPa	YS/MPa	Enhancement factor	Hardening ratio	Toughness*/MPa	Total elongation/%
14Al	638	398	…	1·7	136	21
14Al–ODS–Ti	1169	895	2·2	1·3	94	10
20Al	588	434	…	1·3	113	23
20Al–ODS–Ti	897	610	1·4	1·5	88	12

*Toughness measured as area under the tensile curve.

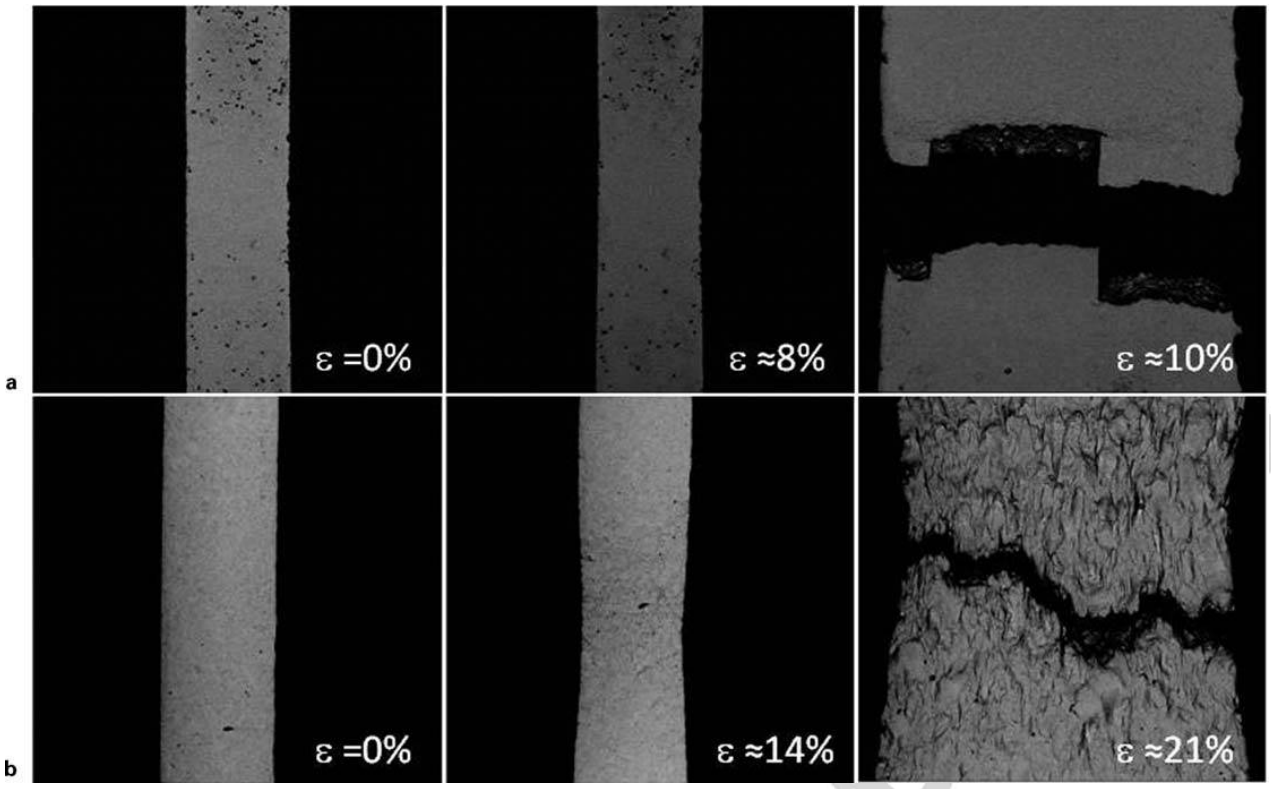

13 Images of tensile tests *in situ* of *a* 14Al–ODS–Ti and *b* prealloyed alloys; from left to right: start of test, necking formation and after failure

loss in efficiency for the tungsten hardening. Regarding the total elongation and toughness the difference is small between both alloys. It is to be noted that in spite of a higher strengthening in 14Al–ODS–Ti no decrease in toughness is noted.

The different behaviour between the ODS and the prealloyed samples is also demonstrated by the in situ tensile tests (Fig. 13). The necking of the tensile specimen gauge is only evidenced in the non ODS materials. Therefore the ODS sample has a catastrophic failure with a very low necking formation in comparison with the prealloyed sample with a sizable necking and a ductile rupture mode. The grains become elongated near the fracture surface for the non-ODS materials while the texture of the grains changes little for the ODS materials (Fig. 13). These results can be compared with results obtained in the work carried out by Hernández-Mayoral *et al.*[21]

Microhardness test

The ODS alloys consolidated by SPS have a higher microhardness than prealloyed alloys. This fact confirms that it has been produced the hardening of the ODS alloy owes to the grain size reduction through ODS processing and also to the efficient sold solution strengthening and to the formation of nanoprecipitates. The comparison between both grades (ODS or not) reflects the difference seen in the tensile testing and discussed above. Present microhardness results compare well with others reported in the literature.[22,23]

Conclusions

The effectiveness of MA and SPS to produce nanostructured powders based on the prealloyed grade Fe and introducing different alloying elements have been evaluated in this work. The morphology and grain size of the milled powders are practically kept in the ODS alloys after their consolidation. The addition of Y_2O_3 and Al promote the formation of Y–Al complex nano-oxides (Y_xAl_yOz) in the ODS alloys. In addition, other types of nano-oxides have been found due to W and Ti addition, bigger than the Y–Al–O oxides. The nanoprecipitates dispersion is responsible for the enhancement of tensile properties and hardness in ODS alloys compared to non-ODS. Comparing both ODS grades the 14Al–ODS–Ti alloy shows better mechanical properties than the 20–Al–ODS–Ti due to a smaller grain size and to a more efficient solid solution strengthening by W when it is incorporated in the melt for the atomization process to obtain the prealloyed grade, than when the alloying is performed by mechanical milling.

All results demonstrate that the SPS can be a promising consolidation technique to produce ODS

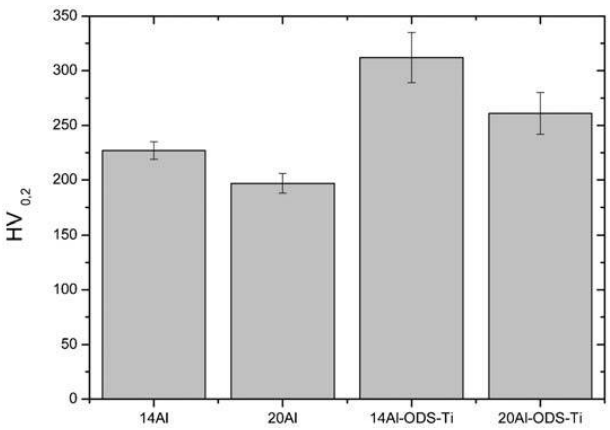

14 Microhardness of alloys consolidated by SPS

alloys nanostructured keeping the structure of milled powders.

Acknowledgements

This investigation has been supported by the Ministerio de Ciencia e Innovación de España through the Project ENE2009-13766-C04-03. The authors would like to thank the Dr Fabrice Gaslain for its contribution during the of EBSD analysis.

References

1. R. L. Klueh, J. P. Shingledecker, R. W. Swindeman and D. T. Hoelzer: *J. Nucl. Mater.*, 2005, **341**, 103–114.
2. R. L. Klueh, D. S. Gelles, S. Jitsukawa, A. Kimura, G. R. Odette, B. van der Schaaf and M. Victoria: *J. Nucl. Mater.*, 2002, **307–311**, (1), 455–465.
3. J. H. Lee, R. Kasada, A. Kimura, T. Okuda, M. Inoue, S. Ukai, S. Ohnuki, T. Fujisawa and F. Abe: *J. Nucl. Mater.*, 2011, **417**, 1225–1228.
4. M. F. S. Ukai: *J. Nucl. Mater.*, 2002, **307–311**, 749–757.
5. M. Ratti, D. Leuvrey, M. H. Mathon and Y. de Carlan: *J. Nucl. Mater.*, 2009, **386–388**, 540–543.
6. S. O. S. Kim, T. Kaito, S. Yamashita, M. Inoue, T. Asayama and T. Shobu: 2011, **417**, 209–211.
7. A. Kimura, R. Kasada, N. Iwata, H. Kishimoto, C. H. Zhang, J. Isselin, P. Dou, J. H. Lee, N. Muthukumar, T. Okuda, M. Inoue, S. Ukai, S. Ohnuki, T. Fujisawa and T. F. Abe: *J. Nucl. Mater.*, 2011, **417**, 176–179.
8. C. L. Chen, A. Richter, R. Kögler and G. Talut: *J. Nucl. Mater.*, 2011, **412**, 350–358.
9. M. K. Miller and C. M. Parish: *Mater. Sci. Technol.*, 2011, **27**, 729–734.
10. J. M. Torralba, L. Fuentes-Pacheco, N. García-Rodríguez and M. Campos: *Adv. Powder Technol.*, 2013, **24**, 813–817.
11. G. Ji, T. Grosdidier, N. Bozzolo and S. Launois: *Intermetallics*, 2007, **15**, 108–118.
12. Y. H. Zhao, Y. Z. Guo, Q. Wei, T. D. Topping, A. M. Dangelewicz, Y. T. Zhu, T. G. Langdon and E. J. Lavernia: *Mater. Sci. Eng. A*, 2009, **A525**, 68–77.
13. P. Olier, M. Couvrat, C. Cayron, N. Lochet and L. Chaffron: *J. Nucl. Mater*.
14. S. Ohtsuka, S. Ukai, M. Fujiwara, T. Kaito and T. Narita: *J. Nucl. Mater. A*, 2004, **329A–333A**, 372–376.
15. P. Olier, M. Couvrat, C. Cayron, N. Lochet and L. Chaffron: *J. Nucl. Mater.*, 2013, **442**, S106–S111.
16. L. Fuentes-Pacheco and M. Campos: *Powder Metall.*, 2012, **55**, 287–293.
17. A. Molinari, S. Libardi, M. Leoni and P. Scardi: *Acta Mater.*, 2010, **58**, 963–966.
18. P. He, M. Klimenkov, R. Lindau and A. Möslang: *J. Nucl. Mater.*, 2012, **428**, 131–138.
19. L. Hsiung, M. Fluss, S. Tumey, J. Kuntz, B. El-Dasher, M. Wall, B. Choi, A. Kimura, F. Willaime and Y. Serruys: *J. Nucl. Mater.*, 2011, **409**, 72–79.
20. R. Kasada, N. Toda, K. Yutani, H. S. Cho, H. Kishimoto and A. Kimura: *J. Nucl. Mater. A*, 2007, **367A–370A**, 222–228.
21. M. Hernández-Mayoral, M. Serrano, E. Oñorbe, A. García-Junceda, I. Hilger, B. Kloeden, T. Weissgaerber, A. Ulbricht, F. Bergner, B. Radiguet, A. Etienne, A. Shariq and C. D. Dewhurst: DOI: http://dx.doi.org/10.1179/1743284714Y.0000000555.
22. M. J. Alinger, G. R. Odette and D. T. Hoelzer: *Acta Mater.*, 2009, **57**, 392–406.
23. N. B. Z. Oksiuta: *Nucl. Fusion*, 2009, **49**, 9.
24. Z. Oksiuta and N. Baluc: *J. Nucl. Mater.*, 2009, **386–388**, 426–429.